nature chemistry

Article

https://doi.org/10.1038/s41557-024-01497-x

Methylation enables the use of fluorine-free ether electrolytes in high-voltage lithium metal batteries

Received: 7 March 2023

Accepted: 28 February 2024

Published online: 03 April 2024

Check for updates

Ai-Min Li[1], Oleg Borodin[2], Travis P. Pollard[2], Weiran Zhang[1], Nan Zhang[1], Sha Tan[3], Fu Chen[4], Chamithri Jayawardana[5], Brett L. Lucht[5], Enyuan Hu[3], Xiao-Qing Yang[3] & Chunsheng Wang[1]

Lithium metal batteries represent a promising technology for next-generation energy storage, but they still suffer from poor cycle life due to lithium dendrite formation and cathode cracking. Fluorinated solvents can improve battery longevity by improving LiF content in the solid–electrolyte interphase; however, the high cost and environmental concerns of fluorinated solvents limit battery viability. Here we designed a series of fluorine-free solvents through the methylation of 1,2-dimethoxyethane, which promotes inorganic LiF-rich interphase formation through anion reduction and achieves high oxidation stability. The anion-derived LiF interphases suppress lithium dendrite growth on the lithium anode and minimize cathode cracking under high-voltage operation. The Li^+-solvent structure is investigated through in situ techniques and simulations to draw correlations between the interphase compositions and electrochemical performances. The methylation strategy provides an alternative pathway for electrolyte engineering towards high-voltage electrolytes while reducing dependence on expensive fluorinated solvents.

The energy density of lithium metal batteries (LMBs) is particularly attractive when paired with high-energy cathodes such as lithium nickel cobalt aluminium oxides (NCAs) due to the high specific capacity (3,860 mAh g^{-1}) and low electrochemical potential (−3.04 V versus the standard hydrogen electrode) of lithium metal anode[1–3]. However, transferring commercial carbonate electrolytes to LMBs yields a poor cycle life, arising from large lithium volume change (dendrite growth) and cathode cracking[4,5]. The mixed organic–inorganic solid–electrolyte interphase (SEI) and cathode electrolyte interphase (CEI) formed in these traditional electrolytes is lithiophilic. The ideal SEI/CEI should be lithiophobic with weak binding to both electrodes to reduce the stress induced by electrode volume changes, and the CEI should also be stable while operating under high voltages. Lithium fluoride (LiF) stands out due to its high lithiophobicity and anodic stability (>6.0 V versus Li/Li^+)[6]; however, simultaneously tailoring LiF-rich SEI/CEI interphases is a difficult task. Advances in tailoring SEIs have been made by promoting fluorinated anion reduction or using fluorinated solvents[7]. 1,2-dimethoxyethane (DME) ether is a popular choice to suppress solvent reduction; however, the α-H atoms of ether molecules are prone to attack by nucleophiles such as singlet oxygen or superoxide species[8–10], resulting in low oxidation stability. The anodic stability of DME electrolytes is markedly improved with lithium bis(fluorosulfonyl)imide (LiFSI)-based highly concentrated electrolytes (HCEs)[11–14] or through the introduction of 'inert' fluorinated diluents (localized HCEs)[15,16], enabling lithium coulombic efficiency (CE) to reach 99.5% (ref. 17). The anodic stability of the DME-based electrolytes can also be enhanced

[1]Department of Chemical and Biomolecular Engineering, University of Maryland, College Park, MD, USA. [2]Battery Science Branch, DEVCOM Army Research Laboratory, Adelphi, MD, USA. [3]Chemistry Division, Brookhaven National Laboratory, Upton, NY, USA. [4]Department of Chemistry and Biochemistry, University of Maryland, College Park, MD, USA. [5]Department of Chemistry, University of Rhode Island, Kingston, RI, USA. e-mail: cswang@umd.edu

https://doi.org/10.1038/s41557-024-01497-x

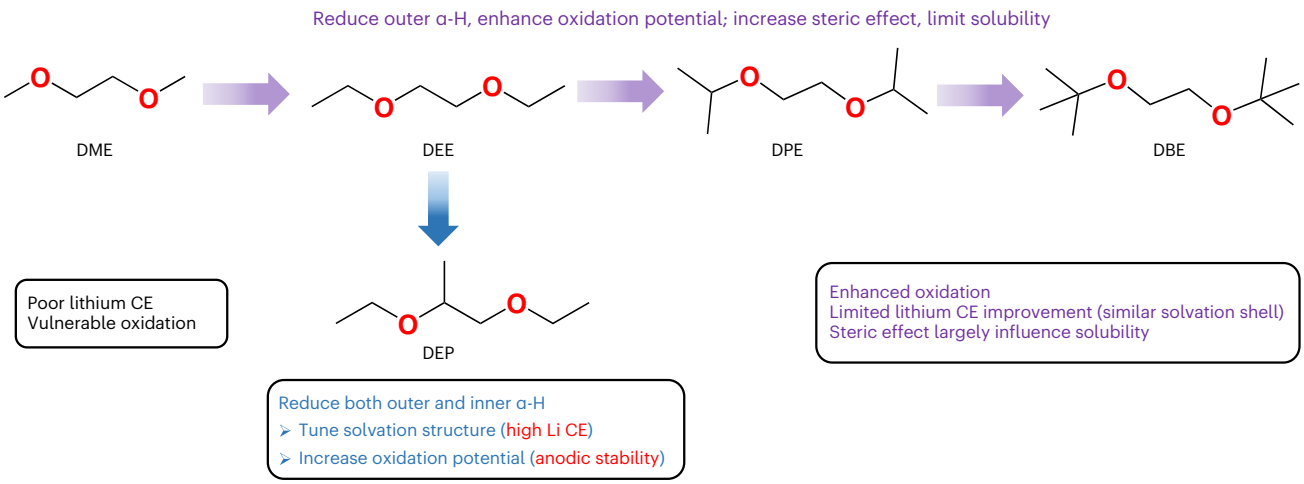

Fig. 1 | Methylation design on DME molecules to enhance the electrochemical performance when formulating electrolytes with LiFSI salt. The horizontal magenta flow indicates the stepwise replacement of outer α-H atoms on DME molecules, which will enhance the molecular oxidation stability with increased steric effects. The salt solubility will also be reduced due to the large spatial hindrance. The methylation of two outer and one inner DME α-H atoms shown in the vertical cyan flow leads to aggregated solvations that result in high Li efficiency and improved anodic stability.

by using fluorinated analogues[18,19], enabling an identical lithium CE of 99.5%, and Li||NMC811 full cells to reach 270 cycles[19]. Although fluorination of ether solvents increases the molecular oxidation potential, it also reduces electrolyte ionic conductivity and cost, posing environmental challenges[20,21]. Alternative strategies using non-fluorinated functional groups[22–24] (which confer enhanced anodic stability while overcoming the limitations of HCEs), localized HCEs and fluorinated solvents are desirable for the long cycle performance of LMBs.

Herein we evaluated a series of solvents by selective methylation of DME α-H atoms (Fig. 1) to tune the molecule's solvation capability, ionic transport, Li^+ desolvation rate and electrochemical stability. The single-salt, single-solvent 2.0 M LiFSI/1,2-diethoxypropane (DEP) electrolytes enable a lithium plating/stripping CE of ~99.7%. When paired with high-voltage NCA cathodes, the electrolytes achieve a high cycle CE of 99.8% with 80% capacity retention over 600 cycles. Furthermore, 100 mAh Li||NCA (4.0 mAh cm^{-2}, N/P = 1) pouch cells with 5 g Ah_E^{-1} lean electrolytes achieve 95% capacity retention after 150 cycles. Finally, the 2.0 M LiFSI/DEP electrolytes enable a record-breaking 250 cycles for anode-free Cu||NCA (4.0 mAh cm^{-2}, N/P = 0) coin cells (Supplementary Tables 1 and 2). The proposed methylation scheme provides a design strategy for LMBs that stabilizes both lithium metal anode and NCA cathode without sacrificing ionic conductivity, increasing cost or imposing environmental concerns.

Results and discussion

Design of methylated DME electrolytes

In this work we showed that the methylation of DME α-H atoms to form 1,2-diethoxyethane (DEE) and 1,2-dipropoxyethane (DPE) increases the spatial effects of the solvents coordinating Li^+, resulting in increased ionic aggregation that promotes the formation of anion-derived LiF-rich SEI and simultaneously enhances the anodic stability of the electrolytes (Fig. 1); however, the increase in the steric effects also reduces salt solubility in these solvents (for example, excluding di-tert-butoxyethane (DBE) for electrolyte formulation), reducing the ionic conductivity (Supplementary Fig. 1). To balance the anti-oxidation capability and ionic conductivity, we selectively methylated one inner and two outer DME α-H atoms to form 1,2-diethoxypropane (DEP), which promotes LiF-rich SEI while preserving high ionic conductivity and high voltage stability in the LiFSI/DEP electrolytes. The substitution of the terminal α-H by methyl groups rather than fluorine functions also enhances molecular oxidation stability without increasing its reduction potential, which reduces the prevalence of organic components in the SEI, making it more lithiophobic, thus effectively suppressing Li dendrite growth.

Properties of methylated DME electrolytes

The oxidation stability of the solvents (DME, DEE, DPE, DBE and DEP) and their corresponding 2.0 M LiFSI electrolytes (except for DBE) were evaluated chemically in a highly oxidized environment and electrochemically facing high-voltage electrodes. The chemical oxidation of the neat solvents was examined by mixing the solvents with suspended KO_2, and the compositions of the oxidized solutions were further evaluated through ^{1}H-NMR spectroscopy (Supplementary Note 1 and Supplementary Figs. 2–9)[25–27]. The result showed that the removal of DME α-H atoms (at both the outer and inner positions) could effectively inhibit the oxidation process and protect the solvents from degradation, which is further validated through density functional theory (DFT) calculations with the increase in the nucleophilic attack reaction barrier following the order of DME < DEP (CH_2) ≈ DEE < DPE < DBE ≪ DEP (propyl CH_3) (Supplementary Fig. 10)[10,28]. The electrochemical stability of the solvents (DME, DEE, DPE and DEP) was also investigated in the 2.0 M LiFSI electrolytes at a high voltage of 4.2 V against both inactive electrodes (Ti) by holding Li||Ti cells at 4.2 V for 24 h, and active electrodes (NCA) by charging/discharging Li||NCA cells between 4.2 V and 2.8 V for 20 cycles (see Supplementary Note 1 for details). Although the electrochemical oxidation mechanism of the electrolytes in Li||NCA cells is different from the chemical degradation of the neat solvents in the presence of KO_2, the same trends were observed with solvent degradation signals decreased in the order of DME < DEE < DPE < DEP electrolytes (Supplementary Fig. 8).

The methylation of DME α-H atoms results in more resistance to oxidation for the formulated 2.0 M LiFSI electrolytes, and the bulky methyl groups also bring a huge steric effect that largely reduces the solvation energy, altering the physical and electrochemical properties of the corresponding electrolytes (Supplementary Table 3). The electrochemical oxidation stability of the four electrolytes (2.0 M LiFSI in DME, DEE, DPE and DEP) was evaluated using linear sweep voltammetry (LSV) in the Li||Al half cells. As expected, the DME electrolytes showed the worst oxidation stability with a large current increase starting at 4.1 V (Fig. 2a, black line). The oxidation stability of DEE electrolytes slightly improves to 4.6 V (Fig. 2a, blue line). Remarkably, considerable high-voltage tolerance was observed for DPE and DEP electrolytes with the onset oxidation voltages pushed up to ~5.3 V (Fig. 2a, green and

https://doi.org/10.1038/s41557-024-01497-x

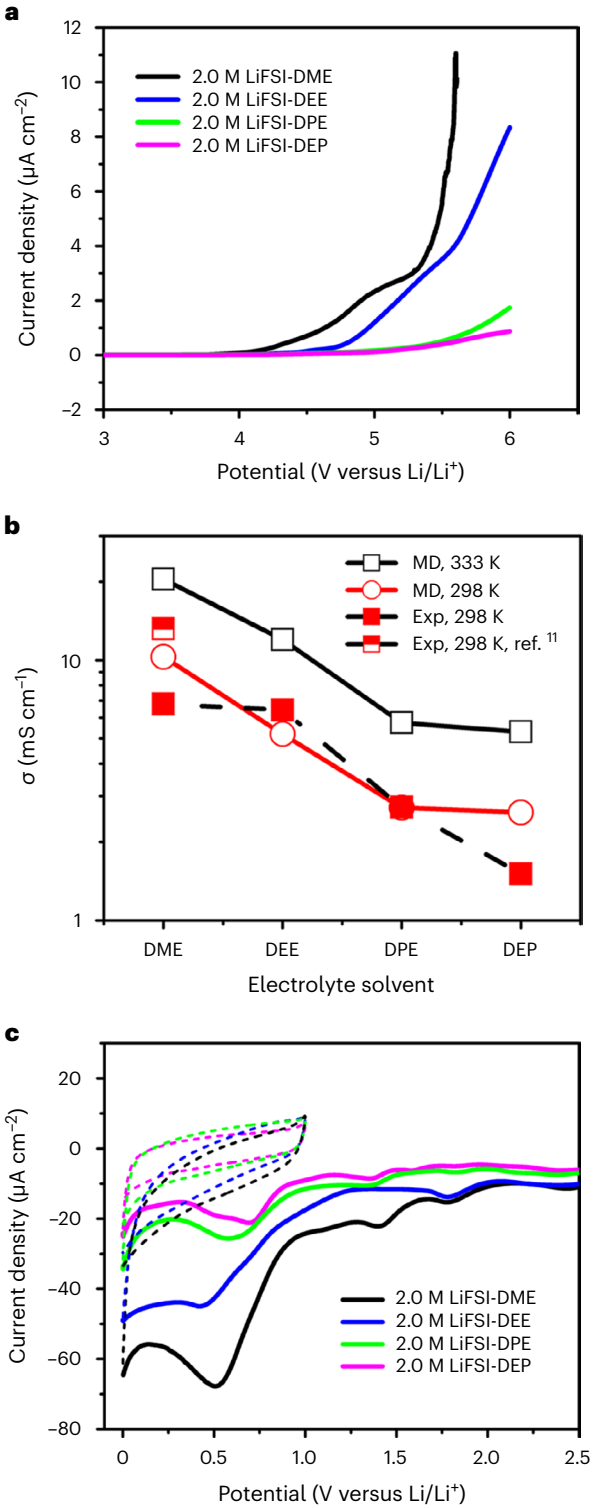

Fig. 2 | Electrochemical performance of 2.0 M LiFSI electrolytes using different solvents. a, LSV anodic scanning in the Li||Al half cells at a scan rate of 0.5 mV s^{-1}. **b**, Ionic conductivity measured at room temperature. The data are compared with molecular dynamic (MD) simulations as well as the reported value for 2.0 M LiFSI-DME (ref. 11). **c**, Cyclic voltammetry cathodic scanning in the Li||Cu half cells at a scan rate of 0.5 mV s^{-1}. The first scan proceeds from the open circuit potential to 0 V versus Li/Li^+ (solid lines), whereas the following scans are between 1.0 and 0 V versus Li/Li^+ (dashed lines).

magenta lines), indicating their compatibility with NCA cathodes. The ionic conductivity decreases in the order of DME > DEE > DPE > DEP as a result of the progressively weaker Li^+–solvent interactions as the solvent donor number decreases from 20 (DME) to 19.3 (DEE) to 18.7 (DPE) to 18.3 (DEP), leading to a lower degree of ion uncorrelated motion (ionicity) due to a stronger ion association (Supplementary Figs. 11 and 12). Yet the DEP electrolytes have sufficient ionic conductivity of >1.5 mS cm^{-1} at room temperature (Fig. 2b) to support battery operation. The reduction behaviour of the electrolytes was also investigated using cyclic voltammetry in the Li||Cu half cells. As shown in Fig. 2c, the methylation of DME α-H atoms greatly decreased the reduction currents. The reduction current decreases with successive methylation of DME α-H atoms from DME, DEE and DPE to DEP electrolytes because the weak solvation increases contact ion pair (CIP) and aggregate (AGG) formation such as [FSI^-–Li^+–FSI^-], which promotes LiF-rich SEI formation with reduced electrolyte degradation[29]. All four solvents (DME, DEE, DPE and DEP) showed very similar HOMO/LUMO energies and reduction/oxidation potentials for both neat solvents and Li^+(solvent) solvates (Supplementary Note 2 and Supplementary Table 4). However, the products of C–O bond cleavage on cathodes after dehydrogenation are different for these solvents, with by-products of DME decomposition more likely to gas out (Supplementary Figs. 13 and 14)[28]. Salt aggregation increases in the order of DME < DEE < DPE < DEP, which promotes the formation of [$Li^+_2(FSI^-)$] AGGs in DEP electrolytes. The decomposition of [$Li^+_2(FSI^-)$] AGGs will form LiF CEIs at the fully/nearly discharged cathode surfaces[29], resulting in the lower anodic current density for electrolytes with DEP versus DME and DEE (Fig. 2a).

Solvation structure of methylated DME electrolytes

The solvation structure of the electrolytes was first investigated using Raman spectroscopy. The S–N–S stretching vibrations mode of the FSI^- anion is observed in the 680–780 cm^{-1} frequency range and is sensitive to the chemical environment (Supplementary Fig. 15)[30,31]. The spectra were deconvoluted to peaks centred at ~720 cm^{-1} (yellow line, solvent-separated ion pairs (SSIPs)), 731 cm^{-1} (green line, CIPs) and 739 cm^{-1} (magenta line, AGGs). The fraction of SSIPs decreases from 59.8% (DME), 45.3% (DEE) and 33.3% (DPE) to 13.9% (DEP), whereas the fraction of AGGs increases from 9.5% (DME), 11.1% (DEE) and 21.7% (DPE) to 58.6% (DEP). The fraction of CIPs follows the same trend as for the AGGs, demonstrating that the methylation of DME α-H atoms increases the number of AGGs and CIPs in the electrolytes, promoting the reduction of FSI^- anions to form a LiF-rich SEI. To further investigate the correlations between the FSI^--anion environment and Raman spectra, we performed DFT calculations on the isolated FSI^- anion and various solvates extracted from molecular dynamics simulations (Supplementary Notes 3 and 4 and Supplementary Fig. 16) for the DEP electrolytes. Calculated Raman frequencies for the bidentate Li^+/FSI^- CIPs are mostly located in the 731–749 cm^{-1} region, partially overlapping with the frequencies for AGGs at 741–755 cm^{-1} with a minor contribution at 733 cm^{-1}, which is largely in line with CIP and AGG fits of the experimental data.

The multinuclear (^{7}Li, ^{19}F, ^{17}O) NMR is very sensitive to the solvation environment[32–34]. A downfield shift of the ^{7}Li and ^{19}F signals is observed as solvents change from DME, DEE and DPE to DEP (Supplementary Fig. 17a,b)[35]. Density functional theory calculations predict the same trend for ^{7}Li shifts as experiments (Supplementary Note 5 and Supplementary Fig. 18a) but indicate that changes in the Li^+-solvate packing for SSIP are largely responsible for the observed trends. The cation–solvent/anion interactions can also be monitored using ^{17}O-NMR because the LiFSI/ether electrolytes only have two groups of oxygen atoms: ethereal oxygen from the solvent and sulfonyl oxygen from the FSI^- anion[36]. The ethereal oxygen shift of the four neat solvents are −21.7 ppm (DME), 7.7 ppm (DEE), 29.5 ppm (DPE) and 29.8 and 6.2 ppm (DEP), aligning with their coordination ability as reflected by their donor numbers (Supplementary Figs. 11 and 17c). Upon adding LiFSI salts, all ethereal oxygen signals get broadened and move upfield to different degrees, indicating different oxygen nuclei environments. Density functional theory calculations demonstrated

https://doi.org/10.1038/s41557-024-01497-x

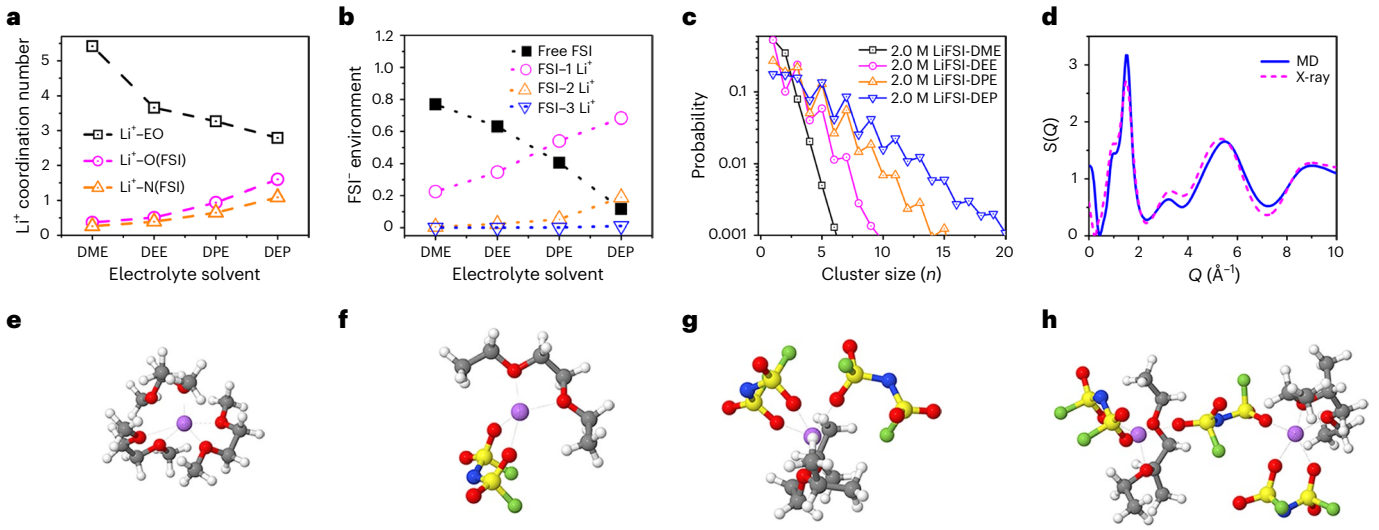

Fig. 3 | Molecular dynamics solvation investigation of the studied electrolytes. **a**–**c**, Ion environments. **a**, Li^+ cation coordination numbers. **b**, The number of Li^+ cations coordinating FSI^- anions (see legend) and the Li^+-FSI^- coordination number $n(Li^+\text{-}FSI^-)$. **c**, The ion cluster size distribution. **d**, Structure factor of LiFSI/DEP electrolytes from molecular dynamics simulations and X-ray measurements. **e**,**f**, Selected lithium solvates for different electrolytes from molecular dynamics simulations. **e**, SSIP of $[Li(DME)_3]^+$. **f**, CIP of {[Li(DEE)](FSI)}. **g**, CIP of $\{[Li(DPE)](FSI)_2\}^-$. **h**, AGG of {[Li(DEP)(FSI)](FSI)[Li(DEP)(FSI)]}$^-$.

a strong dependence of the ether oxygen shifts not only on the Li^+ complexation but also on the solvent conformations (Supplementary Fig. 18b,c and Supplementary Table 5) indicating challenges with the interpretation of experimental trends. The sulfonyl oxygen signals[37] changed considerably: the ^{17}O resonance centred at 170.9 ppm for DME electrolytes, followed by a decrease for DEE (169.3 ppm), and then gradually increased from DPE (170.2 ppm) to DEP (172.2 ppm) (Supplementary Fig. 19). The downfield shift in ^{17}O-NMR correlates with the enrichment of CIPs/AGGs from DEE to DPE and DEP. Furthermore, 2D heteronuclear Overhauser enhancement spectroscopy (HOESY) was also employed to describe the short- (cation–solvent) and long-range (anion–solvent) interactions at the molecular level in a site-resolved manner[38,39]. The 2D {^{7}Li–^{1}H} HOESY spectra reveal that the cation–solvent interactions, and dipolar contacts between lithium cations and specific protons in the solvents can be identified (Supplementary Fig. 20). The increase in cross-peak intensities is attributable to the increasing number of {^{7}Li–^{1}H} spin pairs contributing to the observed spectral intensity. The sum ratio between inner and outer hydrogen atoms (I/O) for DME, DEE, DPE and DEP is calculated to be 0.67, 1.33, 0.50 and 0.78, respectively (Supplementary Fig. 20). The inner and outer hydrogen atoms in DME shared a similar contour plot at I/O of 0.67 due to the rigid configuration of $-CH_3$ (Supplementary Fig. 20a). The intensified overlapping signals of {^{1}H(inner)–^{7}Li} plotted in DEE correlated well with an I/O of 1.33, which corresponds to a higher inner hydrogen population versus the outer population (Supplementary Fig. 20b). The DPE and DEP also follow the I/O trend with an enlarged correlation for the outer hydrogen atoms (Supplementary Fig. 20c,d). A further pictorial view of the anion–solvent interactions is monitored through the 2D {^{19}F–^{1}H} HOESY spectra (Supplementary Fig. 21). The well-distributed FSI^- anion in LiFSI/DME electrolytes leads to similar spatial interactions between the inner and outer hydrogen atoms with the fluorine atoms (Supplementary Fig. 21a). The aggregates of FSI^- anions with Li^+ centres make the fluorine atoms in the AGGs cluster preferentially closer to the non-polar part of the solvents (outer hydrogen atoms), which can be reflected in the increased correlation intensity between the outer hydrogen atoms and the fluorine atoms from DEE, DPE to DEP electrolytes (Supplementary Fig. 21c,d). By the combination of 2D {^{7}Li–^{1}H} and {^{19}F–^{1}H} HOESY experiments, the increasing proximity of FSI^- anion with Li^+ centres was observed from DME, DEE, DPE to DEP electrolytes, providing strong evidence for the evolution of Li^+–FSI^- aggregates with the methylation design strategy.

Molecular dynamics simulations and X-ray diffraction further probed the electrolyte solvation structure (Supplementary Note 4, Fig. 3 and Supplementary Figs. 22–30). Molecular dynamics simulations showed that Li^+ is primarily coordinated by ether oxygen (EO) atoms and FSI^- anion oxygen with coordination numbers shown in Fig. 3a. The Li^+–EO coordination monotonically decreases, whereas Li^+–O (FSI) increases in the solvent order of DME < DEE < DPE < DEP. The fraction of free Li^+ cations (not coordinated to N(FSI) within 5.0 Å) is similar for DME and DEE electrolytes but drops appreciably for DPE and DEP electrolytes (Supplementary Fig. 25). The fraction of Li^+ bound to two FSI^- anions is very small for DME but increases in the order of DME < DEE < DPE < DEP. The fractions of free FSI^-, as well as FSI^- coordinated to one, two and three Li^+ cations (Fig. 3a), also indicate increased aggregation and decreased population of free FSI^- ions from DME to DEE to DPE and DEP, which is in excellent agreement with the Raman analysis (Supplementary Fig. 15). Figure 3c shows a progressively larger cluster formation as solvent changes in the order of DME, DEE, DPE and DEP. Finally, the structure factor of DEP/LiFSI electrolytes predicted from molecular dynamics simulations is in excellent agreement with X-ray data (Fig. 3d), indicating the ability of the force field to reproduce the solvation structure in DEP electrolytes. The high consistency between molecular dynamics simulations, Raman and 1D/2D NMR spectra verify our electrolyte design principle: steric effects from progressive methylation allow more FSI^- anions to participate in the first solvation shell around Li^+ cations. The effect is especially great with the methylation of inner ethylene glycol hydrogen atoms, producing the AGG-rich solvation structure that is beneficial for the long cycle performance of LMBs (Fig. 3e–h).

Lithium plating/stripping in the investigated electrolytes

The electrolyte design principles are further verified experimentally by high Li plating/stripping CE measured using Li||Cu half cells. As shown in Fig. 4a, under complete plating/stripping conditions at a current density of 0.5 mA cm^{-2} and capacity of 1.0 mAh cm^{-2}, the initial Li CE improved from 69.12% (DME), 73.83% (DEE) and 83.84% (DPE) to 95.33% in DEP electrolytes. Cycle-to-cycle efficiencies in the DME electrolytes were notably variable, reaching an average cycle efficiency of only 98.09% in 100 cycles. By contrast, DEE, DPE and DEP electrolytes

https://doi.org/10.1038/s41557-024-01497-x

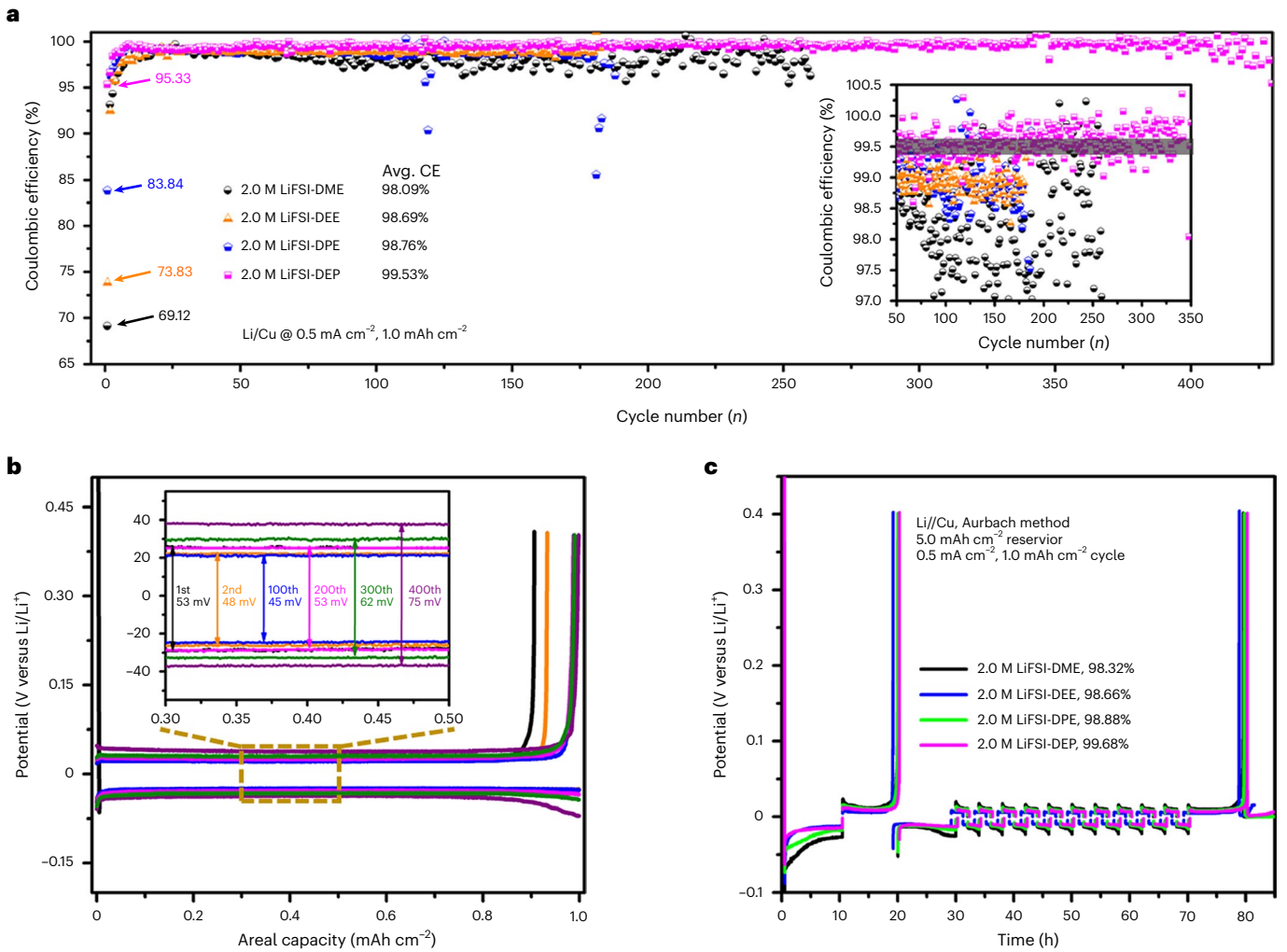

Fig. 4 | Lithium plating/stripping in methylated DME/LiFSI electrolytes. **a**, Lithium plating/stripping under complete plating/stripping conditions in Li||Cu half cells among different electrolytes at 0.5 mA cm^{-2}, 1 mAh cm^{-2}. The inset shows the magnified CEs from 50 to 350 cycles, with a grey bar marking the 99.5% value. **b**, Lithium plating/stripping profiles in DEP electrolytes at the 1st, 2nd, 100th, 200th, 300th and 400th cycles. The inset displays the enlarged voltage profiles with overpotential highlighted for comparison. **c**, Modified Aurbach's measurement of Li metal CE with different electrolytes.

reached higher average cycle efficiencies of 98.69%, 98.76% and 99.53% at 180, 180 and 400 cycles, respectively (Fig. 4a), demonstrating the superior cycling stability of DEP electrolytes with a low overpotential (Fig. 4b). Furthermore, the Aurbach method test, which better evaluates the efficiency of Li cycling on a preserved Li substrate[40], also validated the benefits of DEP electrolyte design by showing a substantially improved average cycle efficiency (99.68%) compared with the reference electrolytes of DME (98.32%), DEE (98.66%) and DPE (98.88%) (Fig. 4c). The high average cycle efficiency of 99.68% is one of the highest among state-of-the-art electrolytes[41], verifying the efficacy of DEP electrolyte design principle (Supplementary Table 2).

The morphology of plated Li in Li||NCA (2.0 mAh cm^{-2}, N/P = 2) full cells after 50 cycles at a current of 0.3 C and voltage range of 2.8–4.3 V in different electrolytes was characterized using a scanning electron microscope (SEM). The deposited Li in DME electrolytes showed high porosity with a large surface area (Fig. 5a), resulting in a low Li CE below 99%, which is consistent with reported results[11]. The porosity was reduced after methylation of DME α-H atoms (Fig. 5b,c), Li cycled with DEP electrolytes showed densely packed, flat and large grains (Fig. 5d). A flat and even distribution of Li is beneficial to achieve a high Li CE and long cycle life of LMBs[16,42,43]. The cross-sectional SEM views of the Li anode confirmed Li density variations after cycling in the four electrolytes. Lithium thickness decreased from 112 µm (DME), 93 µm (DEE) and 91 µm (DPE) to 43 µm (DEP) (Fig. 5). The porous Li structure is formed by Li dendrite growth and results in dead Li formation. Due to the strong bonding of organic-rich SEI to Li metal anodes, the organic-rich SEI will be broken during Li stripping and reformed during Li plating, which reduces Li CE and further increases Li porosity. In contrast, the LiF-rich inorganic SEI with high lithiophobicity will suppress Li dendrite growth, and maintain its stability during Li stripping due to the weak bonding of LiF-SEI to Li, which increases Li efficiency and deposited Li density, as demonstrated by the ~43 µm thin Li in DEP electrolytes after 50 cycles (Fig. 5d).

X-ray photoelectron spectroscopy (XPS) with argon sputtering was used to examine the SEI compositions on the cycled Li (Supplementary Figs. 31–36). The SEI in the DME and DEE electrolytes had high C 1*s* intensity (~8%) on the SEI surface, and the organic component increased to 14% after 1 min sputtering depth (Supplementary Fig. 31a,b). However, the SEI in DPE and DEP electrolytes showed lower C 1*s* intensity (~4%) on the surface, which slightly decreased during the sputtering (Supplementary Fig. 31c,d). This result indicates that there is less solvent decomposition on the Li metal surface in DPE and DEP compared with DME and DEE electrolytes. Moreover, the C–C/C–H and C–O/C=O species decrease following the trend of DME, DEE, DPE and DEP (Supplementary Fig. 32), which validates the enhanced inorganic SEI in DEP electrolytes from anion reduction. There is also evidence of the

https://doi.org/10.1038/s41557-024-01497-x

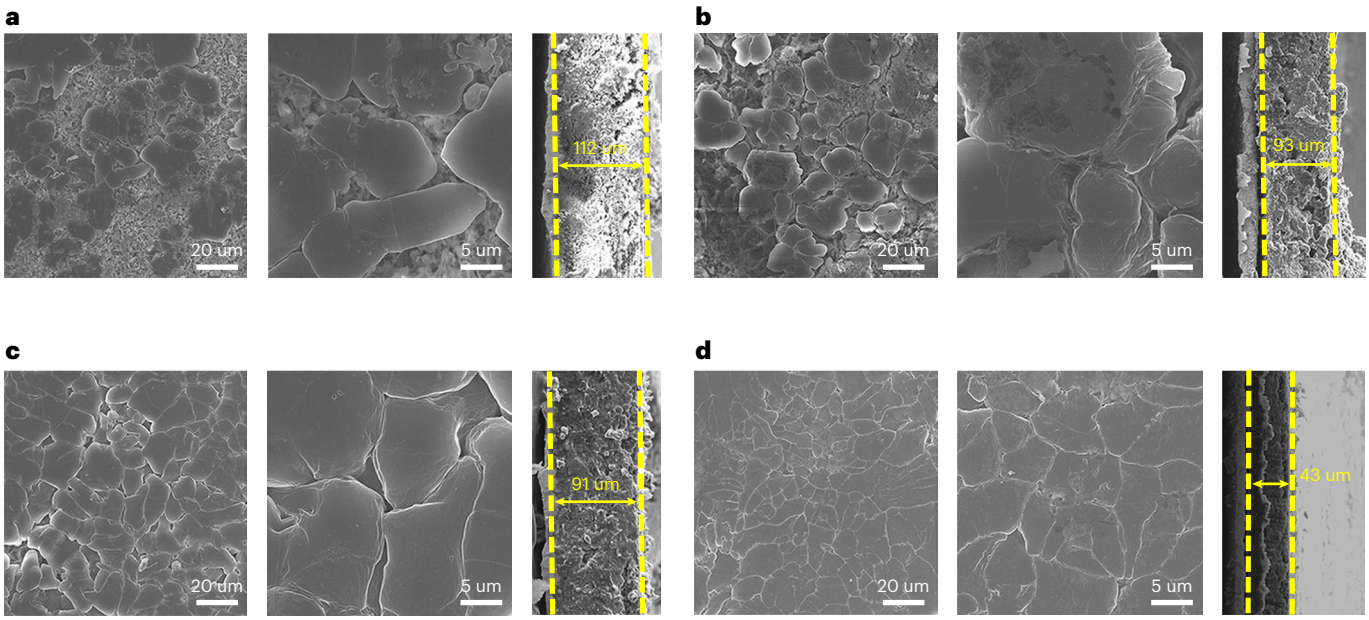

Fig. 5 | Scanning electron microscope images illustrating lithium metal morphology after 50 cycles in Li||NCA cells with the investigated electrolytes. **a**–**d**, DME (**a**), DEE (**b**), DPE (**c**) and DEP (**d**). The left and centre images show the Li morphology at different resolutions, whereas the right images display the cross-sectional views, with the yellow dashed lines marking the evolution of the electrode thickness.

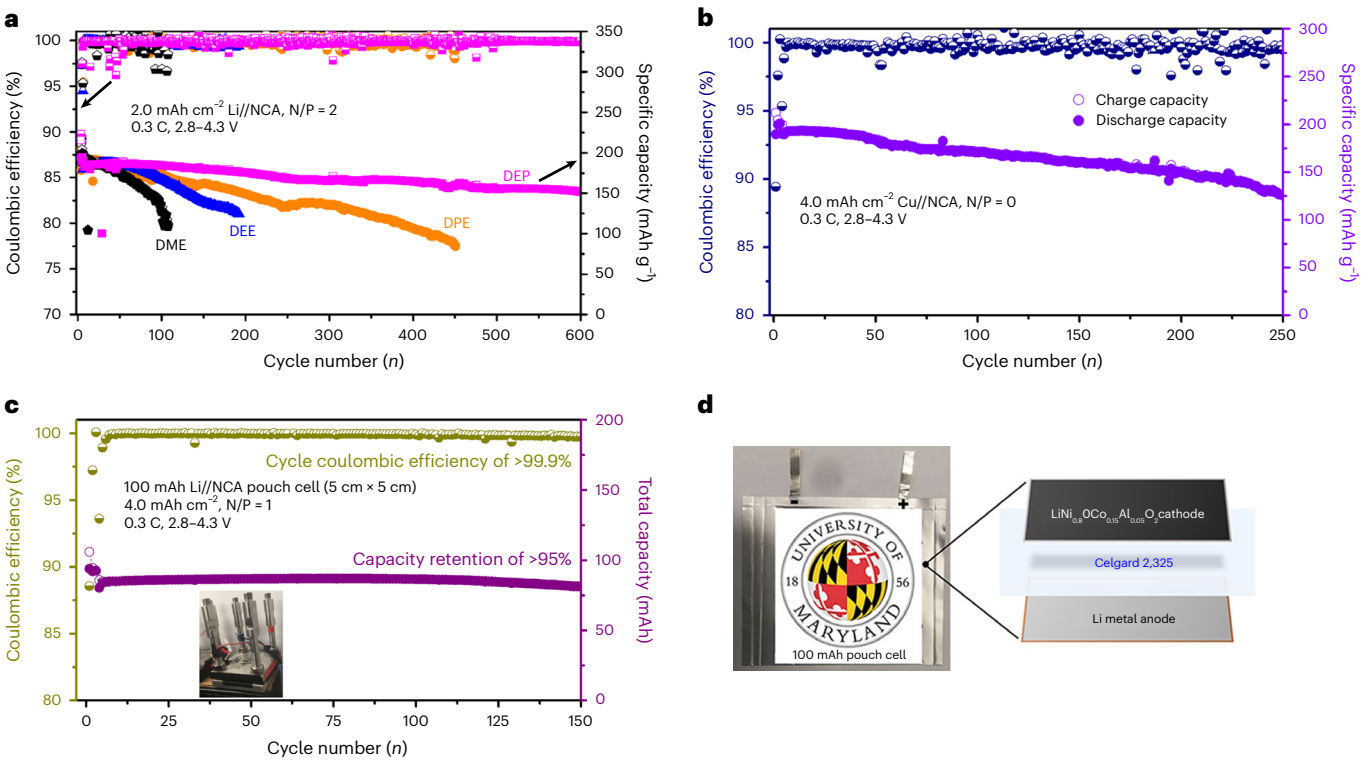

Fig. 6 | Li||NCA full cell performance with different areal loadings and N/P ratios. **a**, Li||NCA (2.0 mAh cm^{-2}, N/P = 2) cells cycled with different electrolytes. **b**, Li-free Cu||NCA (4.0 mAh cm^{-2}, N/P = 0) cells cycled with DEP electrolytes. **c**, 100 mAh home-made pouch cells (4.0 mAh cm^{-2}, N/P = 1) cycled with DEP electrolytes. The inset shows the actual test conditions under room temperature and 0.1 MPa. The CE and specific capacity (total capacity for **c**) are shown on different axes with key features marked in the figure. **d**, The 100 mAh LMBs pouch cells configuration as illustrated.

anion-derived inorganic SEI in the O 1*s* and S 2*p* spectra (Supplementary Figs. 33 and 34). The continuous increase of S_n^{x-} and Li_2O species following the trend of DME, DEE, DPE and DEP indicates that FSI^- anion was preferentially reduced to form the inorganic LiF-Li_2S-Li_2O SEI. The reduction of FSI^- anion results in lithiophobic inorganic-rich SEI, which effectively suppresses Li dendrite growth and increases Li efficiency (Figs. 4 and 5). Furthermore, the inorganic SEI is thin and also has low resistance, which enhances the rate performance of the batteries[44,45].

Performance of Li||NCA, Li-free Cu||NCA coin and pouch cells

We investigated the electrochemical performance of Li||NCA cells with three different N/P ratios (N/P = 2, 1, 0, where Li-free Cu||NCA cells have a N/P ratio of 0). The DEP electrolytes enabled 4.3 V Li||NCA cells (2.0 mAh cm^{-2}, N/P = 2) to achieve ~80% capacity retention after 600 cycles at 0.3 C under a depth of discharge of 100% (Fig. 6a, magenta line, and Supplementary Fig. 37a). However, the DME, DEE and DPE electrolytes can only maintain a capacity of 54%, 63% and 43% at 105, 190 and 450 cycles, respectively (Fig. 6a, black, blue and orange lines, and Supplementary Fig. 37b–d). The fast capacity decay in DME, DEE and DPE electrolytes correlates with the low Li plating/stripping CE (Fig. 4) and venerable oxidation stability (Fig. 2a) among the electrolytes. The anodic stability of DME electrolytes is limited to 4.1 V and showed the worst cell stability. The slightly improved anodic stability of the DEE solvent extended the cycle life to 190 cycles, whereas the high oxidation stability (>5.0 V) of the DPE and DEP electrolytes, and high Li CE (DPE, 98.88%; DEP, 99.68%) improved the cyclability of Li||NCA cells to 450 and 600 cycles, respectively. The high anodic stability and LiF-rich SEI of DEP electrolytes ensure Li||NCA cells achieve a long cycle life of 600 and a high CE of 99.8%. Furthermore, the Li||NCA cells were disassembled at the discharge state after the long cycles (105, 190, 450 and 600 cycles for DME, DEE, DPE and DEP electrolytes, respectively) to investigate the Li morphology. Scanning electron microscopy images showed that the Li morphology differences were further developed compared with the post-mortem analysis at 50 cycles (Fig. 5 and Supplementary Fig. 38). The Li thickness increased to 176 µm (DME), 137 µm (DEE), 115 µm (DPE) and 61 µm (DEP) after the long cycles. Porous and dendritic lithium was observed with DME and DEE electrolytes, correlating to the easy shortage of the long-cycled cells (Fig. 6a and Supplementary Fig. 38a,b). Lithium chunks in DPE electrolytes are found embedded with porous Li fibres, reflecting the low Li CE with organic–inorganic SEI (Fig. 4 and Supplementary Fig. 38c). In contrast, the densely packed Li in DEP electrolytes after 600 cycles demonstrates the effectiveness of LiF-SEI in preventing Li dendrite growth and a smooth Li deposition (Supplementary Fig. 38d). Moreover, the electrochemical performance of Li-free Cu||NCA full cells with a high areal capacity of 4.0 mAh cm^{-2} was also evaluated under lean electrolyte conditions (E/C ratio ≈ 5 g Ah_E^{-1}) (Fig. 6b and Supplementary Fig. 39). The anode-free cells with DEP electrolytes can stably cycle for over 250 cycles with a high capacity retention of >61.7%, which is the record performance in all reported anode-free cells (Supplementary Table 1). Moreover, single-layer 100 mAh Li||NCA pouch cells with an areal capacity of 4.0 mAh cm^{-2} and a low N/P ratio of ~1 were also assembled and evaluated between 2.8 V and 4.3 V at 0.3 C. As shown in Fig. 6c,d, the high-energy Li||NCA pouch cells under lean DEP electrolytes conditions (E/C ratio ≈ 5 g Ah_E^{-1}) showed a superior cycle performance with >95% capacity retention after 150 cycles with negligible voltage polarization (Supplementary Fig. 40).

Conclusion

Compared with carbonate electrolytes, ether-based electrolytes exhibit better stability at Li metal anodes; however, the low anodic stability of ether molecules hinders their application in high-voltage LMBs. Through selective methylation of DME α-H atoms, we were able to simultaneously increase the Li plating/stripping CE to >99.7% and improve the electrolyte anodic stability up to 5 V. The aggregate-dominated solvation of 2.0 M LiFSI-DEP electrolytes was demonstrated through in situ Raman, 1D multinuclear and 2D heteronuclear NMR spectroscopy, and molecular dynamics simulations. DEP electrolytes demonstrated excellent cycle performance for 4.3 V Li||NCA (2.0 mAh cm^{-2}, N/P = 2) full cells (600 cycles with CE of 99.8%), 100 mAh Li||NCA (4.0 mAh cm^{-2}, N/P = 1) pouch cells (95% capacity retention after 150 cycles), and Li-free Cu||NCA (4.0 mAh cm^{-2}, N/P = 0) full cells to achieve a record cycle life of 250. The methylation of DME α-H atoms provides an alternative pathway for electrolyte engineering towards high-voltage electrolytes with ether-based solvents while reducing dependence on expensive fluorinated solvents.

Online content

Any methods, additional references, Nature Portfolio reporting summaries, source data, extended data, supplementary information, acknowledgements, peer review information; details of author contributions and competing interests; and statements of data and code availability are available at https://doi.org/10.1038/s41557-024-01497-x.

References

1. Liu, J. et al. Pathways for practical high-energy long-cycling lithium metal batteries. *Nat. Energy* **4**, 180–186 (2019).
2. Cao, Y. et al. Bridging the academic and industrial metrics for next-generation practical batteries. *Nat. Nanotechnol.* **14**, 200–207 (2019).
3. Choi, J. W. & Aurbach, D. Promise and reality of post-lithium-ion batteries with high energy densities. *Nat. Rev. Mater.* **1**, 16013 (2016).
4. Albertus, P. et al. Status and challenges in enabling the lithium metal electrode for high-energy and low-cost rechargeable batteries. *Nat. Energy* **3**, 16–21 (2017).
5. Tikekar, M. D., Choudhury, S., Tu, Z. & Archer, L. A. Design principles for electrolytes and interfaces for stable lithium-metal batteries. *Nat. Energy* **1**, 16114 (2016).
6. Fan, X. et al. Fluorinated solid electrolyte interphase enables highly reversible solid-state Li metal battery. *Sci. Adv.* **4**, eaau9245 (2018).
7. Fan, X. et al. Non-flammable electrolyte enables Li-metal batteries with aggressive cathode chemistries. *Nat. Nanotechnol.* **13**, 715–722 (2018).
8. McLafferty, F. W. Mass spectrometric analysis of aliphatic ethers. *Anal. Chem.* **29**, 1782–1789 (1957).
9. Sun, W. et al. Insights into the oxidation kinetics of a cetane improver—1,2-dimethoxyethane (1,2-DME) with experimental and modeling methods. *Proc. Combust. Inst.* **37**, 555–564 (2019).
10. Di Tommaso, S., Rotureau, P. & Adamo, C. Oxidation mechanism of aliphatic ethers: theoretical insights on the main reaction channels. *J. Phys. Chem. A* **116**, 9010–9019 (2012).
11. Qian, J. et al. High rate and stable cycling of lithium metal anode. *Nat. Commun.* **6**, 6362 (2015).
12. Jiao, S. et al. Stable cycling of high-voltage lithium metal batteries in ether electrolytes. *Nat. Energy* **3**, 739–746 (2018).
13. Zheng, J. et al. Manipulating electrolyte and solid electrolyte interphase to enable safe and efficient Li–S batteries. *Nano Energy* **50**, 431–440 (2018).
14. Suo, L. et al. A new class of solvent-in-salt electrolytes for high-energy rechargeable metallic lithium batteries. *Nat. Commun.* **4**, 1481 (2013).
15. Chen, S. et al. High-voltage lithium-metal batteries enabled by localized high-concentration electrolytes. *Adv. Mater.* **30**, 1706102 (2018).
16. Cao, X. et al. Monolithic solid–electrolyte interphases formed in fluorinated orthoformate-based electrolytes minimize Li depletion and pulverization. *Nat. Energy* **4**, 796–805 (2019).
17. Cao, X. et al. Effects of fluorinated solvents on electrolyte solvation structures and electrode/electrolyte interphases for lithium metal batteries. *Proc. Natl Acad. Sci. USA* **118**, 2020357118 (2021).
18. Yu, Z. et al. Molecular design for electrolyte solvents enabling energy-dense and long-cycling lithium metal batteries. *Nat. Energy* **5**, 526–533 (2020).
19. Yu, Z. et al. Rational solvent molecule tuning for high-performance lithium metal battery electrolytes. *Nat. Energy* **7**, 94–106 (2022).
20. Ajanovic, A. & Haas, R. Economic and environmental prospects for battery electric- and fuel cell vehicles: a review. *Fuel Cells* **19**, 515–529 (2019).

21. Bai, Y. et al. Energy and environmental aspects in recycling lithium-ion batteries: concept of battery identity global passport. *Mater. Today* **41**, 304–315 (2020).
22. Chen, Y. et al. Steric effect tuned ion solvation enabling stable cycling of high-voltage lithium metal battery. *J. Am. Chem. Soc.* **143**, 18703–18713 (2021).
23. Park, E. et al. Exploiting the steric effect and low dielectric constant of 1,2-dimethoxypropane for 4.3 V lithium metal batteries. *ACS Energy Lett.* **8**, 179–188 (2022).
24. Sharon, D. et al. 2,4-Dimethoxy-2,4-dimethylpentan-3-one: an aprotic solvent designed for stability in Li–O_2 cells. *J. Am. Chem. Soc.* **139**, 11690–11693 (2017).
25. Camacho-Forero, L. E. & Balbuena, P. B. Elucidating electrolyte decomposition under electron-rich environments at the lithium-metal anode. *Phys. Chem. Chem. Phys.* **19**, 30861–30873 (2017).
26. Freunberger, S. A. et al. The lithium-oxygen battery with ether-based electrolytes. *Angew. Chem. Int. Ed.* **50**, 8609–8613 (2011).
27. Bryantsev, V. S. et al. Predicting solvent stability in aprotic electrolyte Li–air batteries: nucleophilic substitution by the superoxide anion radical ($O_2^{\bullet-}$). *J. Phys. Chem. A* **115**, 12399–12409 (2011).
28. Bryantsev, V. S. et al. The identification of stable solvents for nonaqueous rechargeable Li-air batteries. *J. Electrochem. Soc.* **160**, A160 (2012).
29. Alvarado, J. et al. Bisalt ether electrolytes: a pathway towards lithium metal batteries with Ni-rich cathodes. *Energy Environ. Sci.* **12**, 780–794 (2019).
30. Xie, J. D. et al. Superior Coulombic efficiency of lithium anodes for rechargeable batteries utilizing high-concentration ether electrolytes. *Electrochim. Acta* **319**, 625–633 (2019).
31. Chen, S. et al. High-efficiency lithium metal batteries with fire-retardant electrolytes. *Joule* **2**, 1548–1558 (2018).
32. Hayashi, K. et al. Dependence of lithium metal secondary cell performance on lithium cation solvation state. *J. Power Sources* **81**, 782–785 (1999).
33. Thielen, J. et al. Multinuclear NMR study of structure and mobility in cyclic model lithium conducting systems. *Appl. Magn. Reson.* **45**, 1063–1073 (2014).
34. Deng, X. et al. Natural abundance ^{17}O nuclear magnetic resonance and computational modeling studies of lithium-based liquid electrolytes. *J. Power Sources* **285**, 146–155 (2015).
35. Ma, P., Mirmira, P. & Amanchukwu, C. V. Effect of building block connectivity and ion solvation on electrochemical stability and ionic conductivity in novel fluoroether electrolytes. *ACS Cent. Sci.* **7**, 1232–1244 (2021).
36. Wan, C. et al. Natural abundance ^{17}O, ^{6}Li NMR and molecular modeling studies of the solvation structures of lithium bis(fluorosulfonyl)imide/1,2-dimethoxyethane liquid electrolytes. *J. Power Sources* **307**, 231–243 (2016).
37. Ren, X. et al. Enabling high-voltage lithium-metal batteries under practical conditions. *Joule* **3**, 1662–1676 (2019).
38. Martin, P. A. et al. Correlating intermolecular cross-relaxation rates with distances and coordination numbers in ionic liquids. *J. Phys. Chem. Lett.* **9**, 7072–7078 (2018).
39. Kumar, V. et al. Lithium speciation in the $LiPF_6$/PC electrolyte studied by two-dimensional heteronuclear Overhauser enhancement and pulse-field gradient diffusometry NMR. *J. Phys. Chem. C* **123**, 9661–9672 (2019).
40. Aurbach, D., Youngman, O. & Dan, P. The electrochemical behavior of 1,3-dioxolane—$LiClO_4$ solutions—II. Contaminated solutions. *Electrochim. Acta* **35**, 639–655 (1990).
41. Hobold, G. M. et al. Moving beyond 99.9% Coulombic efficiency for lithium anodes in liquid electrolytes. *Nat. Energy* **6**, 951–960 (2021).
42. Xue, W. et al. Ultra-high-voltage Ni-rich layered cathodes in practical Li metal batteries enabled by a sulfonamide-based electrolyte. *Nat. Energy* **6**, 495–505 (2021).
43. Fang, C. et al. Quantifying inactive lithium in lithium metal batteries. *Nature* **572**, 511–515 (2019).
44. Guo, R. & Gallant, B. M. Li_2O solid electrolyte interphase: probing transport properties at the chemical potential of lithium. *Chem. Mater.* **32**, 5525–5533 (2020).
45. May, R. et al. Rapid interfacial exchange of Li ions dictates high Coulombic efficiency in Li metal anodes. *ACS Energy Lett.* **6**, 1162–1169 (2021).

Methods

Materials and electrolytes preparation

LiFSI (>99.99%) salt was purchased from Gotion Company. DME (reagent grade >99%) and DEE (98%) were purchased from Sigma-Aldrich, and dried over activated molecular sieves (4 Å, Sigma-Aldrich) before use. The DEP, DBE and DEP solvents were synthesized through three different reaction routes (please refer to Supplementary Figs. 41–46 for synthetic details and characterizations). Saft America kindly provided the $LiNi_{0.8}Co_{0.15}Al_{0.05}O_2$ (NCA) cathodes coated on aluminium foil with areal loadings of 2.0 and 4.0 mAh cm^{-2}. The ultrathin Li foil with a controlled thickness of 20 µm was purchased from MTI Corp. The 2.0 M LiFSI electrolyte solutions were prepared by dissolving 2.0 mmol LiFSI salt in 1.0 ml corresponding dried solvents under a moisture-free inert environment in an argon-filled glovebox at 25 °C. Homogeneous and clear solutions were obtained by careful hand-shaking of the vials. The prepared electrolytes were filtered through 0.5 µm PTFE syringe filters before usage.

Characterization

NMR spectra (^{1}H–, ^{13}C–, ^{19}F–, ^{17}O–, ^{7}Li–) were recorded at 25 °C on Bruker 400 MHz high-resolution spectrometers with D_2O or C_6D_6 as deuterated solvents. Two-dimensional HOESY experiments (^{7}Li–^{1}H, and ^{19}F–^{1}H) were performed on Bruker Avance III HD 400 MHz spectrometers equipped with a broadband fluorine observe probe. NMR data were processed using Bruker TopSpin software (v.4.1.4; https://www.bruker.com/en/products-and-solutions/mr/nmr-software/topspin.html). The electrode morphologies were characterized using a Hitachi SU-70 field emission gun SEM or a JEOL 2100 F field emission scanning transmission electron microscope. The Horiba Jobin Yvon Labram Aramis with a 532 nm diode-pumped solid-state laser was used for Raman data collection. X-ray photoelectron spectroscopy data were collected with K-Alpha X-ray Photoelectron Spectrometer System (Thermo Scientific, aluminium Kα radiation, $h\nu$ = 1486.68 eV) at the University of Rhode Island. The tested electrodes (Li on Cu foils or NCA cathodes, disassembled after cycling) were washed with the corresponding parent solvents for 30 s to remove the remaining electrolytes and vacuum-dried before mounting the samples for testing. The samples were directly moved from the argon atmosphere to the XPS chamber with a vacuum transfer container to avoid any exposure to the air. The depth profiling was conducted using an Ar^+ ion gun with an ion energy of 200 eV. The etching procedure was carried out in a cycle of accumulated 0, 60, 120, 180, 300 and 600 s. All data were referenced to the C 1*s* peak with a binding energy value of 284.8 eV. Peak fitting and relative atomic percentage estimation were performed with CasaXPS software (v.2.3.25)[46], after the removal of a Shirley background and accounting for the relative sensitivity factors of Thermo Kα. The pair distribution function measurements were carried out at the 28-ID-2 beamline of National Synchrotron Light Source II in Brookhaven National Laboratory using a photon wavelength of 0.1818 Å. The obtained data were integrated using Fit2D software (v.18)[47]. The pair distribution function and $G(r)$ values were extracted using PDFgetX3 (v.2.1.2) software[48].

Electrochemical measurements

All of the battery parts used in this work are commercially available, and electrochemical tests were performed in a 2032-type coin-cell, aluminium-clad CR2032 coin-cell, or pouch-cell configurations. All cells were fabricated in an argon-filled glovebox (O_2 and H_2O < 0.1 ppm) and one layer of Celgard 2325 separator was used. Linear sweep voltammetry and cyclic voltammetry with different voltage ranges were conducted on a CHI 600E electrochemical workstation (CH Instruments). The anodic LSV tests were performed over the 3.0 to 6.0 V range in Li||Al cells at a scan rate of 0.5 mV S^{-1}. All of the charge–discharge processes of Li||Cu, Li||NCA and Cu||NCA in the coin cells were tested using a Wuhan LAND Electronic Company CT2001A tester. Pouch-cell cycling was performed on an Arbin battery test station (BT2000, Arbin Instruments). For galvanostatic tests of NCA coin cells, NCA cathodes with a diameter of 12.7 mm (0.5 inch) were coupled with 20-µm-thickness lithium or pure copper as the anode. The total amount of the electrolyte solution was controlled at 30 or 50 µl. All of the electrochemical measurements were conducted at room temperature (25 to 27 °C). Li^+ transference number, and electrochemical impedance spectroscopy were tested on a Gamry 1000E electrochemical workstation. The electrochemical impedance spectroscopy measurements were taken over a frequency range of 1 MHz to 0.1 Hz.

Statistics and reproducibility

No statistical method was used to predetermine the sample size.

Data availability

We declare that the data supporting the findings of this study are available within the article and its Supplementary Information. An archive containing a final configuration from molecular dynamics simulations, force field, simulation parameters and molecular dynamics code is provided. Source data are provided with this paper.

References

46. Fairley, N. et al. Systematic and collaborative approach to problem solving using X-ray photoelectron spectroscopy. *Appl. Surf. Sci.* **5**, 100112 (2021).
47. Hammersley, A. P. FIT2D: a multi-purpose data reduction, analysis and visualization program. *J. Appl. Crystallogr.* **49**, 646–652 (2016).
48. Qiu, X., Thompson, J. W. & Billinge, S. J. L. PDFgetX2: a GUI-driven program to obtain the pair distribution function from X-ray powder diffraction data. *J. Appl. Crystallogr.* **37**, 678 (2004).

Acknowledgements

This work was supported by the US Department of Energy (DOE) under award no. DE-EE0008202 (C.W.) & DE-SC0023408 (C.W.) at the University of Maryland (UMD). The work at Brookhaven National Laboratory is supported by the Assistant Secretary for Energy Efficiency and Renewable Energy, Vehicle Technology Office of the US Department of Energy (DOE) through the Advanced Battery Materials Research (BMR) Program under contract no. DE-SC0012704 (E.H. and X.-Q.Y.). This research used 28-ID-2 beamline of the National Synchrotron Light Source II, US DOE Office of Science User Facilities, operated for the DOE Office of Science by Brookhaven National Laboratory under contract no. DE-SC0012704 (E.H. and X.-Q.Y.). Modelling work was supported by DEVCOM ARL and the Center for Research on Extreme Batteries (O.B.).

Author contributions

A.-M.L. and C.W. conceived the idea for the project and wrote the paper. O.B. and T.P.P. conducted and analysed the DFT calculations and molecular dynamics simulations and also assisted with paper revision and mechanism identification. W.Z and N.Z. assisted with electrochemical cell tests. F.C. helped with the NMR set-up. C.J. and B.L.L. helped with the XPS data collection. S.T., E.H. and X.-Q.Y. helped with the synchrotron data collection and analysis. All of the authors discussed the results and analysed the data.

Competing interests

The authors declare no competing interests.

Additional information

Supplementary information The online version contains supplementary material available at https://doi.org/10.1038/s41557-024-01497-x.

Correspondence and requests for materials should be addressed to Chunsheng Wang.

Peer review information *Nature Chemistry* thanks JianZhi Hu and the other, anonymous, reviewer(s) for their contribution to the peer review of this work.